Journal of Materials Chemistry B

ROYAL SOCIETY OF CHEMISTRY

PAPER

View Article Online
View Journal | View Issue

Cite this: J. Mater. Chem. B, 2025, 13, 4855

Glycosylated polyplex micelles from oppositely charged block copolymers†

Mokun Chen,[ab] Théophile Pelras,[a] Joël Benninga,[ab] Vincent S. D. Voet,[b] Rudy Folkersma[b] and Katja Loos *[a]

Received 12th December 2024,
Accepted 22nd March 2025

DOI: 10.1039/d4tb02760d

rsc.li/materials-b

Glycosylated nanoparticles hold significant promise for applications in biomedicine, because of their ability to mimic complex carbohydrate interactions. Herein, we report the synthesis of block copolymers featuring both a glycosylated segment and a charged block *via* RAFT polymerization and postpolymerization modifications. Additionally, we prepared glycosylated polyplex micelles by mixing oppositely charged glycosylated block copolymers in aqueous media. Electrostatic interactions between the charged segments occur, triggering the formation of glycosylated nanoparticles with a polyplex core. The resulting nanoparticles were characterized *via* dynamic light scattering (DLS), ζ-potential measurements and transmission electron microscopy (TEM), which confirmed their nonspherical morphology. Furthermore, we expanded this strategy by incorporating oppositely charged homopolymers, highlighting the versatility of our approach. These findings demonstrate a robust and modular platform for the design of glycosylated nanoparticles, paving the way for future exploration of their dynamic properties and potential use as responsive carriers for drug delivery.

Introduction

Carbohydrates are ubiquitous in nature, and play crucial roles as energy storage[1] (*e.g.*, glycogen and starch) and as structural material[2–4] (*e.g.*, cellulose, chitin and collagen). Most importantly, carbohydrates are involved in numerous biomolecular recognition events, including the inflammatory response and microbial or viral infections, due to their ability to selectively and specifically bind to proteins located on the surface of cells. Although the monovalent interaction between a monosaccharide and its receptor is relatively weak, the multivalent interactions offered by carbohydrates, known as the 'cluster glycoside effect',[5] significantly increase the overall binding strength. This multivalency leads to greater biological activity, which can be leveraged for applications in recognition processes[6] and drug delivery systems.[7] Polysaccharides, as naturally occurring and highly abundant carbohydrates, possess inherent advantages for use as materials.[8–11] However, their use in biomedical applications can be hampered by challenges such as poor structural control, limited solubility and inherent fragility.

Nature remains a vast source of inspiration, particularly in the field of biomedicine, where mimicking biological behaviors with tailor-made molecules is essential for achieving significant breakthroughs. Glycopolymers, are synthetic analogues of polysaccharides, and feature pendant carbohydrate moieties instead of sugar motifs within the polymer backbone. Glycopolymers have been developed as laboratory-made alternatives that can be more easily produced and tailored. They can be synthesized directly from glycomonomers *via* various polymerization techniques, or sugar moieties can later be attached onto a functional polymer backbone.[12] This enables the facile production of glycopolymers with tailored properties, such as chain length, dispersity or end-group functionality. This degree of control becomes even more important when the synthesis of sequence-controlled glycopolymers, such as glycosylated block copolymers, is sought.

Various glycosylated block copolymers have already been utilized for the production of glycosylated nanoparticles, which can be tailored for a wide range of applications.[13–16] Stenzel *et al.* not only demonstrated the formation of polymer micelles featuring a hydrophobic core and a glycosylated shell, but also investigated their applications for drug delivery. While a hydrophobic drug can be encapsulated and subsequently released from the micellar core,[17] smart macromolecular design can also bring shape-changing capability[18,19] or enzymatic degradability[20] of the nanoparticles. These examples of glycosylated nanoparticles rely on solvophobic interactions for self-assembly, where the hydrophobic block collapses and is stabilized by the hydrophilic

[a] Macromolecular Chemistry and New Polymeric Materials, Zernike Institute for Advanced Materials, University of Groningen, Nijenborgh 3, 9747 AG, The Netherlands. E-mail: k.u.loos@rug.nl
[b] Circular Plastics, Academy Tech & Design, NHL Stenden University of Applied Sciences, 7811 KL Emmen, The Netherlands

† Electronic supplementary information (ESI) available. See DOI: https://doi.org/10.1039/d4tb02760d

glycosylated segment. Additionally, a plethora of alternative self-assembly methods, such as direct hydration,[21–23] polymerization-induced self-assembly,[24,25] sugar deprotection self-assembly[26–28] and temperature induced self-assembly,[29,30] have been reported for the preparation of glycosylated nanoparticles in aqueous media.

Despite its potential, interpolyelectrolyte complexation has been absent from the toolkit for preparing glycosylated nanoparticles. The utilization of electrostatic interactions between oppositely charged polymers is a well-established strategy for the creation of soft materials, particularly in aqueous environments, where the hydrophilicity of charged polymers enhances their functional performance. Complexation between oppositely charged polymers triggers the formation of a largely dehydrated coacervate. Owing to the pseudo-hydrophobic[31] nature of the polyplex domains, particularly when charge-neutrality is achieved, instability occurs and the coacervate tends to precipitate or aggregate. Therefore, the attachment of water-soluble yet charged neutral chains onto polyelectrolytes is necessary to stabilize the particles in water. Before the advent of carbohydrate-decorated polymers, poly(ethylene glycol) was widely used for this purpose,[32,33] even offering a certain degree of biocompatibility, but concerns regarding its immune response,[34,35] as well as the desire to move toward biosourced[14,36] and biodegradable[37] alternatives are opening doors toward the formation of glycosylated polyplex micelles.

In this study, an efficient approach for the construction of glycosylated polyplex micelles *via* electrostatic interactions was demonstrated (Scheme 1). Two block copolymers, each comprising a glycosylated block and a charged segment, were synthesized *via* a combination of sequential reversible addition–fragmentation chain-transfer (RAFT) polymerization and postpolymerization modification techniques. Through stoichiometric mixing of the block copolymer solutions, nanoparticles with a polyplex core (*i.e.*, a complex formed between the charged segments) and stabilized by a glycosylated corona were successfully formed. The resulting nanoparticles were characterized *via* dynamic light scattering (DLS), ζ-potential measurements and transmission electron microscopy (TEM), which confirmed their size and morphology.

Results and discussion

The overall synthesis strategy involves the use of RAFT polymerization to produce a glycopolymer as the macromolecular chain-transfer agent (macro-CTA), which is then chain-extended to incorporate poly(2-(dimethylamino)ethyl methacrylate), followed by deprotection to expose the glucose units, and quaternization to yield a glycopolymer containing a strong polycationic block. An alternative pathway involves chain extension with poly(*tert*-butyl methacrylate), followed by simultaneous deprotection to obtain a glycopolymer featuring a weak polyanionic segment.

Although glycosylated polymers can be directly synthesized *via* the polymerization of hydrophilic sugar monomers,[38–40] an alternative approach was employed to convert glucose into a hydrophobic protected glycomonomer. This strategy not only facilitates its polymerization and subsequent chain extension reactions but also enables more straightforward characterization of the various polymer intermediates.[41–43] The protected glycomonomer, acetonide-protected glucose methacrylate (PrGlcMA), was synthesized through a two-step reaction: (i) the introduction of two acetonide protective groups onto α-D-glucose, followed by (ii) the addition of a methacrylic moiety to the remaining hydroxyl group. This method enhances both the reactivity and manageability of the monomer during the polymerization process (details are in ESI†). After flash column chromatography, PrGlcMA was obtained at high purity, as confirmed by ^{1}H and ^{13}C nuclear magnetic resonance (^{1}H NMR and ^{13}C NMR, respectively, Fig. S1, ESI†), as well as high-resolution mass spectrometry (Fig. S2, PrGlcMA + Na_{theo} = 351.14142, PrGlcMA + Na_{exp} = 351.14103, ESI†).

The synthesis of glycosylated block copolymers was initiated with the polymerization of PrGlcMA to poly(acetonide protected glucose methacrylate) (PPrGlcMA). RAFT polymerization, which is mediated by 2-cyanopropan-2-yl propyl trithiocarbonate as the CTA, was employed because of its ability to produce polymers with low dispersity, high chain-end fidelity, and compatibility with a wide range of monomers. This particular

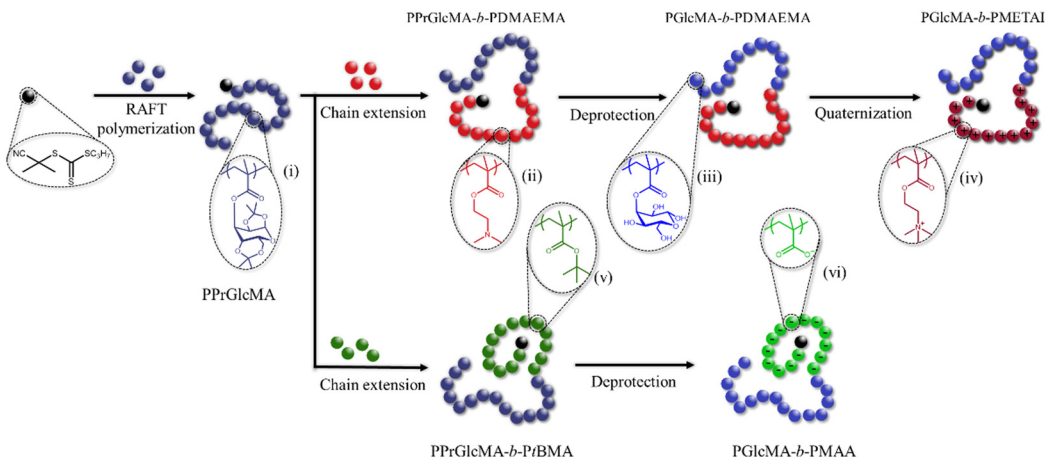

Scheme 1 Synthesis of charged glycosylated block copolymers.

CTA was selected for its enhanced stability, as the trithiocarbonate group is less susceptible to hydrolysis[44] and shows greater resistance to strong nucleophiles, which is crucial for subsequent deprotection steps. Additionally, its short C3 alkane chain is less hydrophobic than that of commercially available C12 CTAs, which is particularly relevant for our hydrophilic diblock copolymers.

The successful synthesis of the glycosylated homopolymer was verified *via* ^{1}H NMR (Fig. 1A$_1$), which allowed for the calculation of the polymer's chain length on the basis of monomer conversion (conv. = 95%, $DP_{PPrGlcMA}$ = 72, $M_{n,NMR}$ = 23 800 Da), while size exclusion chromatography (SEC) was used to monitor the dispersity of the polymers ($Đ$ = 1.56, Fig. 1B). Although featuring a high dispersity, the polymer elugram retains a Gaussian distribution (*i.e.*, absence of chain-chain termination or tailing), suggesting a potential interaction with the column material. Most importantly, an excellent ratio was found between the acetonide signals (12H, 1.33–1.49 ppm) and the glucose ring (7H, 3.68–5.81 ppm), confirming the absence of unwanted deprotection.

Subsequently, chain extension reactions *via* RAFT polymerization were performed to produce different block copolymers. The PPrGlcMA-*block*-poly(2-(dimethylamino)ethyl methacrylate) (PPrGlcMA$_{72}$-*b*-PDMAEMA$_{71}$) block copolymer was synthesized using PPrGlcMA as the macro-CTA. ^{1}H NMR confirmed the introduction of the new block, as evidenced by the new proton signals (CH_2, 2H, 4.05 ppm; CH_2 2H, 2.56 ppm; CH_3, 6H, 2.28 ppm, Fig. 1A$_1$), and enabled the calculation of the degree of polymerization of the second block through monomer conversion (conv. = 71%, $DP_{PDMAEMA}$ = 71, $M_{n,NMR}$ = 35 000 Da). SEC confirmed the chain extension, as indicated by a complete shift of the peak toward a lower retention time and the absence of chain–chain termination, while preserving a reasonable dispersity ($Đ$ = 1.66). The PPrGlcMA-*block*-poly(*tert*-butyl methacrylate) (PPrGlcMA$_{72}$-*b*-P*t*BMA$_{85}$, Fig. 1A$_2$) block was similarly synthesized using PPrGlcMA as the macro-CTA. ^{1}H NMR again confirmed the introduction of the new block, as shown by the appearance of new proton signals (CH_3, 9H, 1.41 ppm, Fig. 1A$_2$), and was used to calculate the degree of polymerization of the second block on the basis of the

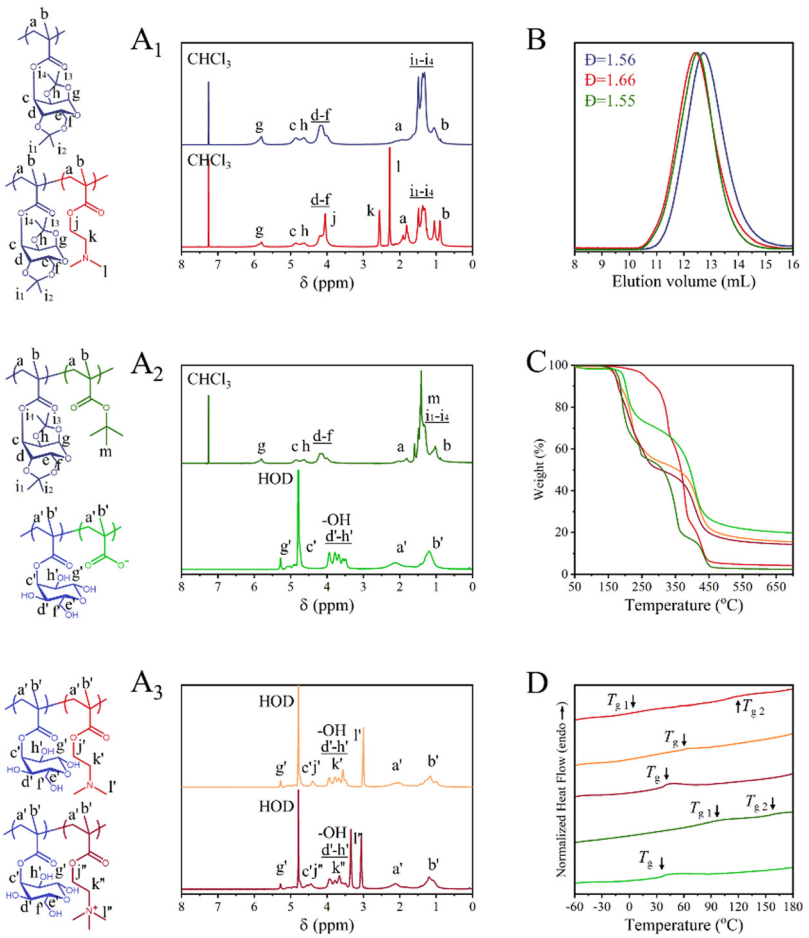

Fig. 1 Characterization of oppositely charged glycosylated block copolymers and their precursors. (A$_1$)–(A$_3$) ^{1}H NMR spectra of the polymers: PPrGlcMA$_{72}$ (dark blue), PPrGlcMA$_{72}$-*b*-PDMAEMA$_{71}$ (red), and PPrGlcMA$_{72}$-*b*-P*t*BMA$_{85}$ (dark green), PGlcMA$_{72}$-*b*-PMAA$_{85}$ (light green), PGlcMA$_{72}$-*b*-PDMAEMA$_{71}$ (orange), PGlcMA$_{72}$-*b*-PMETAI$_{71}$ (dark red). (B) SEC elugrams of PPrGlcMA$_{72}$ (dark blue), PPrGlcMA$_{72}$-*b*-PDMAEMA$_{71}$ (red) and PPrGlcMA$_{72}$-*b*-P*t*BMA$_{85}$ (dark green). (C) TGA and (D) DSC analyses of PPrGlcMA$_{72}$-*b*-PDMAEMA$_{71}$ (red), PGlcMA$_{72}$-*b*-PDMAEMA$_{71}$ (orange), PGlcMA$_{72}$-*b*-PMETAI$_{71}$ (dark red), PPrGlcMA$_{72}$-*b*-P*t*BMA$_{85}$ (dark green) and PGlcMA$_{72}$-*b*-PMAA$_{85}$ (light green).

monomer conversion (conv. = 81%, DP_{PtBMA} = 85, $M_{n,NMR}$ = 35 900 Da). SEC further confirmed the chain extension by complete shift of the peak toward a lower retention time and reasonable dispersity ($Đ$ = 1.55).

The two diblock copolymers, which are currently in their protected and hydrophobic state, require postpolymerization modifications to achieve their desired functionality. While hexafluoroisopronanol/hydrochloric acid has been previously reported as an efficient method for the removal of *tert*-butyl protective groups,[45] trifluoroacetic acid (TFA) has demonstrated the ability to simultaneously remove both acetonide[20,46] and *tert*-butyl groups.[47,48] Preliminary tests on PPrGlcMA and P*t*BMA homopolymers (details are in ESI†) revealed that both routes are viable, with the TFA route yielding slightly better results, as shown by clearer signals of the glucose ring in the ^{1}H NMR spectra (Fig. S4-1, ESI†). This method was first applied to PPrGlcMA$_{72}$-*b*-P*t*BMA$_{85}$ to produce a poly(glucose methacrylate)-*block*-poly(methacrylic acid) (PGlcMA$_{72}$-*b*-PMAA$_{85}$) through a facile two-in-one deprotection step. PGlcMA$_{72}$-*b*-PMAA$_{85}$, now soluble in water, was analyzed by ^{1}H NMR, which confirmed the complete removal of both protective groups, with the disappearance of the acetonide and *tert*-butyl signals (1.18–1.64 ppm, respectively, Fig. 1A$_2$). Fourier-transform infrared spectroscopy (FT-IR, Fig. S5-2, ESI†) also evidenced the loss of the *tert*-butyl protective groups and the appearance of O–H stretching at 3000–3600 cm^{-1}. The same protocol was used to expose the glucose units on PPrGlcMA$_{72}$-*b*-PDMAEMA$_{71}$, yielding water-soluble PGlcMA$_{72}$-*b*-PDMAEMA$_{71}$, which is now soluble in water (Fig. 1A$_3$). To ensure the PDMAEMA segment would remain soluble at any pH, a quaternization step was performed following a previously reported procedure.[47,49] ^{1}H NMR confirmed the modification by the shift of the CH_2 and CH_3 proton signals (from 3.05 to 3.34 ppm), yielding a PGlcMA-*block*-poly(2-(methacryloyloxy)ethyl trimethylammonium iodide) (PGlcMA$_{72}$-*b*-PMETAI$_{71}$) diblock copolymer featuring a strong polyelectrolyte segment.

Thermal characterization was conducted on the various block copolymers and their precursors, beginning with thermogravimetric analysis (TGA, Fig. 1C and Fig. S6, ESI†). The results indicate that none of the protected block copolymers exhibit significant degradation below 180 °C, highlighting the relatively high thermal stability of the acetonide and *tert*-butyl protective groups. PPrGlcMA$_{72}$-*b*-PDMAEMA$_{71}$ demonstrates greater thermal stability, with the initial weight loss occurring at approximately 190 °C, corresponding to the degradation of the acetonide protective groups. PGlcMA$_{72}$-*b*-PDMAEMA$_{71}$ rapidly decomposes above 190 °C because of the removal of protective acetonide groups, and the weight loss is attributed primarily to the degradation of the glucose rings. PGlcMA$_{72}$-*b*-PMETAI$_{71}$ follows a similar decomposition trend, even after quaternization. While PPrGlcMA$_{72}$-*b*-P*t*BMA$_{85}$ demonstrates the earliest onset of degradation, it experiences a rapid weight loss of approximately 40% at approximately 250 °C. This degradation is primarily due to the early decomposition of the *tert*-butyl groups,[50] followed by the subsequent thermolysis or hydrolysis of the remaining polymer. In contrast, after deprotection, PGlcMA$_{72}$-*b*-PMAA$_{85}$ shows improved thermal stability and higher residual mass.

Differential scanning calorimetry (DSC) was performed to assess the thermal behaviour of the block copolymers and their precursors (Fig. 1D and Fig. S6, ESI†). PPrGlcMA$_{72}$-*b*-PDMAEMA$_{71}$ has two distinct glass transition temperatures ($T_{g\,PPrGlcMA\text{-}b\text{-}PDMAEMA\,1}$ = 119 °C and $T_{g\,PPrGlcMA\text{-}b\text{-}PDMAEMA\,2}$ = 5 °C, Table S1, ESI†), which suggests that the blocks do not mix. The higher T_g is attributed to the rigid PPrGlcMA segment ($T_{g\,PPrGlcMA}$ = 150 °C, Table S2, ESI†), whereas the lower T_g corresponds to the softer PDMAEMA segment ($T_{g\,PDMAEMA}$ = 6 °C, Table S2, ESI†). The T_g values of $T_{g\,PPrGlcMA\text{-}b\text{-}PDMAEMA\,1}$ and $T_{g\,PPrGlcMA\text{-}b\text{-}PDMAEMA\,2}$ are lower than the T_g values of individual PPrGlcMA and PDMAEMA, presumably due to block mixing near the interface,[51,52] which increases the mobility of the polymer chains. After deprotection, the PGlcMA segment becomes more flexible ($T_{g\,PGlcMA}$ = 61 °C, Table S2, ESI†), and PGlcMA$_{72}$-*b*-PDMAEMA$_{71}$ features a unique T_g at 62 °C. This suggests either that deprotection enables mixing of the two blocks or that the thermal behavior of the PrGlcMA block prevails over that of the PDMAEMA. Following quaternization, the PMETAI segment becomes more rigid because of stronger interactions between the charged polymer chains ($T_{g\,PMETAI}$ = 48 °C, Table S2, ESI†). PGlcMA$_{72}$-*b*-PMETAI$_{71}$ exhibited a single thermal transition ($T_{g\,PGlcMA\text{-}b\text{-}PMETAI}$ = 40 °C, Table S1, ESI†), possibly due to the mixing of the blocks. The thermogram of PPrGlcMA$_{72}$-*b*-P*t*BMA$_{85}$ shows two distinct transitions ($T_{g\,PPrGlcMA\text{-}b\text{-}PtBMA\,1}$ =153 °C and $T_{g\,PPrGlcMA\text{-}b\text{-}PtBMA\,2}$ = 83 °C, Table S1, ESI†), corresponding to those of the PPrGlcMA ($T_{g\ PPrGlcMA}$ = 150 °C, Table S2, ESI†) and P*t*BMA ($T_{g\,PtBMA}$ = 120 °C, Table S2, ESI†) homopolymers. After deprotection, both segments of PGlcMA$_{72}$-*b*-PMAA$_{85}$ become softer, and polymer exhibits a broad thermal transition near the T_g of the individual polymers ($T_{g\,PGlcMA\text{-}b\text{-}PMAA}$ = 38 °C, Table S1 (ESI†); $T_{g\,PGlcMA}$ = 61 °C and $T_{g\,PMAA}$12= 45 °C, Table S2, ESI†).

The formation of glycosylated polyplex micelles (GPM) was subsequently investigated through electrostatic complexation between oppositely charged PMETAI and PMAA segments (Fig. 2A). Solutions of each block copolymer were prepared at a concentration of 1 g L^{-1} in 10 mM KNO_3 and a pH of 7.2, which permits the $PMAA_{85}$ block to be charged ($pK_{a\,PMAA}$= 4.8–5.5),[53] while the charge of $PMETAI_{71}$ is independent of pH. When aqueous solutions of PGlcMA$_{72}$-*b*-PMAA$_{85}$ and PGlcMA$_{72}$-*b*-PMETAI$_{71}$ (GPM$_1$) were mixed, micelles formed almost instantaneously. A stoichiometric ratio (1 : 1) between the positively charged PMETAI and the negatively charged PMAA segments was used to balance the charges so that a charge-neutral and pseudo hydrophobic domain formed, *i.e.*, the core of the micelles. Dynamic light scattering (DLS) experiments were conducted to measure the effective hydrodynamic radii of the particles. Using this technique, we confirmed the presence of small particles with a mean core diameter of $D_{h\,GPM1}$ = 14.6 nm and a rather low polydispersity index (PDI = 0.149) (Fig. 2B, Fig. S7-1, ESI†). The small diameter may be attributed to the glycosylated corona around the core, as PGlcMA segments not only provide stability and solubility in water but also prevent the micelles from continuously growing into

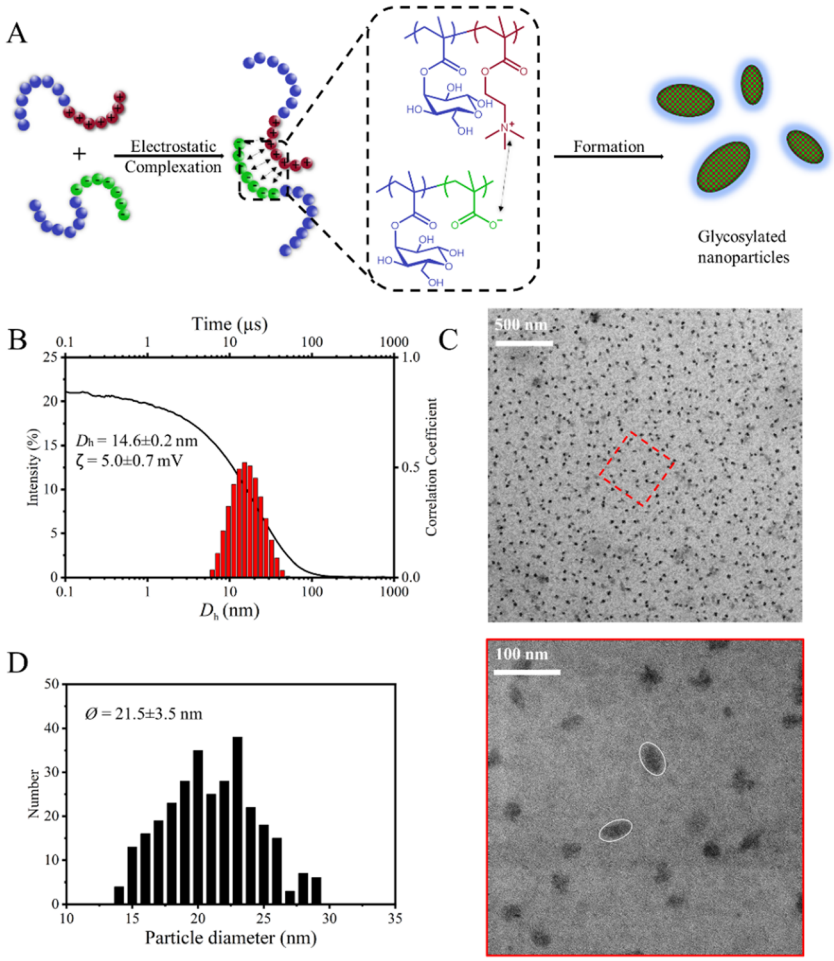

Fig. 2 Formation of glycosylated polyplex micelles through electrostatic complexation between oppositely charged glycosylated block copolymers. (A) Schematic representation of the self-assembly process. (B) DLS (173°) intensity plot (bars) and correlation coefficient (line) of glycosylated nanoparticles in a 10 mM KNO3 solution. (C) TEM images of uranyl acetate-stained glycosylated nanoparticles. (D) Statistical analysis of glycosylated nanoparticles (data extracted from 300 particles in several images).

larger particles.[54] Additionally, the low salt concentration of the solution leads to stronger charge repulsion between polyelectrolytes and results in slower diffusion of the individual polymer molecules in the solution, which inhibits polymer aggregation into larger clusters.[55] ζ-Potential measurements (ζ_{GPM1} = 5.0 mV, Table 1) confirmed the quasi neutral nature of the particles and the near-compensation of all charges. Visualization of the nanoparticles was conducted *via* transmission electron microscopy (TEM) on negatively stained samples (Fig. 2C). Uranyl acetate was used to stain the polyplex domains at the particle cores, resulting in an inverted contrast (*i.e.*, 'positive staining').[56] The particles observed in most samples were elliptical. Polyplex micelles in solution with a nonspherical morphology are not common, and elliptical shape is theoretically predicted as possible intermediates in the transition from spheres to lamellae.[57] Elliptical overall shape and disc-like core formed from the complexation of oppositely charged block copolymers have been reported previously,[58,59] with the proposed mechanism of coronal microphase separation of the stabilizing segments from different block copolymers. For GPM_1, elliptical

Table 1 Characteristics of glycosylated polyplex micelles (GPM)

GPM	Polyanion (x)[a]	Polycation (y)[a]	D_h[b] (nm)	PDI[b]	ζ[b] (mV)	Ø[c] (nm)
GPM_1	$PGlcMA_{72}$-*b*-$PMAA_{85}$ (1)	$PGlcMA_{72}$-*b*-$PMETAI_{71}$ (1)	14.6	0.149	5.0	21.5
GPM_2	$PGlcMA_{72}$-*b*-$PMAA_{85}$ (1)	$PMETAI_{41}$ (1)	63.2	0.142	1.1	50.5
GPM_3	$PMAA_{74}$ (1)	$PGlcMA_{72}$-*b*-$PMETAI_{71}$ (1)	69.5	0.079	6.9	70.9
GPM_4	PSPMA-Na_{114} (1)	$PGlcMA_{72}$-*b*-$PMETAI_{71}$ (1)	89.3	0.092	−18.0	90.4
GPM_5	PSPMA-Na_{114} (0.5)	$PGlcMA_{72}$-*b*-$PMETAI_{71}$ (1)	114.0	0.081	−5.0	96.2

[a] Stoichiometric ratio between the polyanion and the polycation. [b] Determined by DLS/ζ-potential measurements at 25 °C on 1 g L^{-1} solutions in 10 mM KNO_3 and measured in triplicate. [c] Determined from TEM images and measurements of 300 particles.

micelles with constant dimensions were observed on a large scale, suggesting that the PGlcMA corona plays an important role in stabilizing the nonspherical morphology. Additionally, the mean core diameter ($Ø_{GPM1}$ = 21.5 nm) of GPM_1 was obtained from statistical analyses of several TEM images (Fig. 2D). The glycosylated polyplex micelles exhibited a good stability due to their rigid complex core and stabilizing segments. No dissociation or aggregation was observed during measurements.

Since the concept of glycosylated polyplex micelles (GPM) with block copolymers was demonstrated, different polymers have been explored for charge compensation, potentially eliminating the need for glycosylated block copolymers. Three charged homopolymers, $PMETAI_{41}$, $PMAA_{74}$ and poly(sulfopropyl methacrylate) sodium salt ($PSPMA\text{-}Na_{114}$), were produced *via* a combination of RAFT polymerization and postpolymerization modification (details are in ESI†). Two of these polymers, namely, $PMETAI_{41}$ and $PSPMA\text{-}Na_{119}$, are strong polyelectrolytes, *i.e.*, their charge density is pH-independent in the medium, which have significant rigidity and hydrodrynamic volume in water.

The preparation of GPM was conducted as previously described, with the aim of nearly compensating for the charge in 10 mM KNO_3. However, here we used a pair consisting of a glycosylated block copolymer and one complementary homopolymer. Aqueous solutions of $PMETAI_{41}$ and $PGlcMA_{72}$-*b*-$PMAA_{85}$ (GPM_2) were mixed at a 1 : 1 stoichiometric ratio between positively charged PMETAI and negatively charged PMAA segments (Fig. 3A$_1$). This led to the formation of stable and spherical micellar-like polyplexes. ζ-Potential measurements (ζ_{GPM2} = 1.1 mV, Table 1) confirmed the quasi neutrality of the particles' core and the near-compensation of all charges. The DLS results (Fig. 3B$_1$ and Fig. S7-2, ESI†) revealed the presence of glycosylated polyplex micelles with hydrodynamic radius of $D_{h\,GPM2}$ = 63.2 nm, whereas the TEM images (Fig. 3C$_1$) confirmed their spherical morphology with mean core diameters of $Ø_{GPM2}$ = 50.5 nm (Fig. S7-1, ESI†). The hydrodynamic radius from ($D_{h\,GPM2}$) DLS is smaller than the mean core diameter ($Ø_{GPM2}$), possibly due to the hydration layer in DLS or/and particle shrinkage in TEM of the micelles. Interestingly, while the components of GPM_2 are similar to those of GPM_1, the resulting polyplex micelle morphologies are markedly different. The possible reason is that both GPM_1 and GPM_2 initially underwent a transient phase in which metastable large-scale aggregates formed *via* spontaneous complexation after mixing.[60] However, owing to the less stabilizing corona in GPM_2 than in GPM_1, the charge-neutral clusters of GPM_2 underwent thermodynamic equilibration.[61] This process

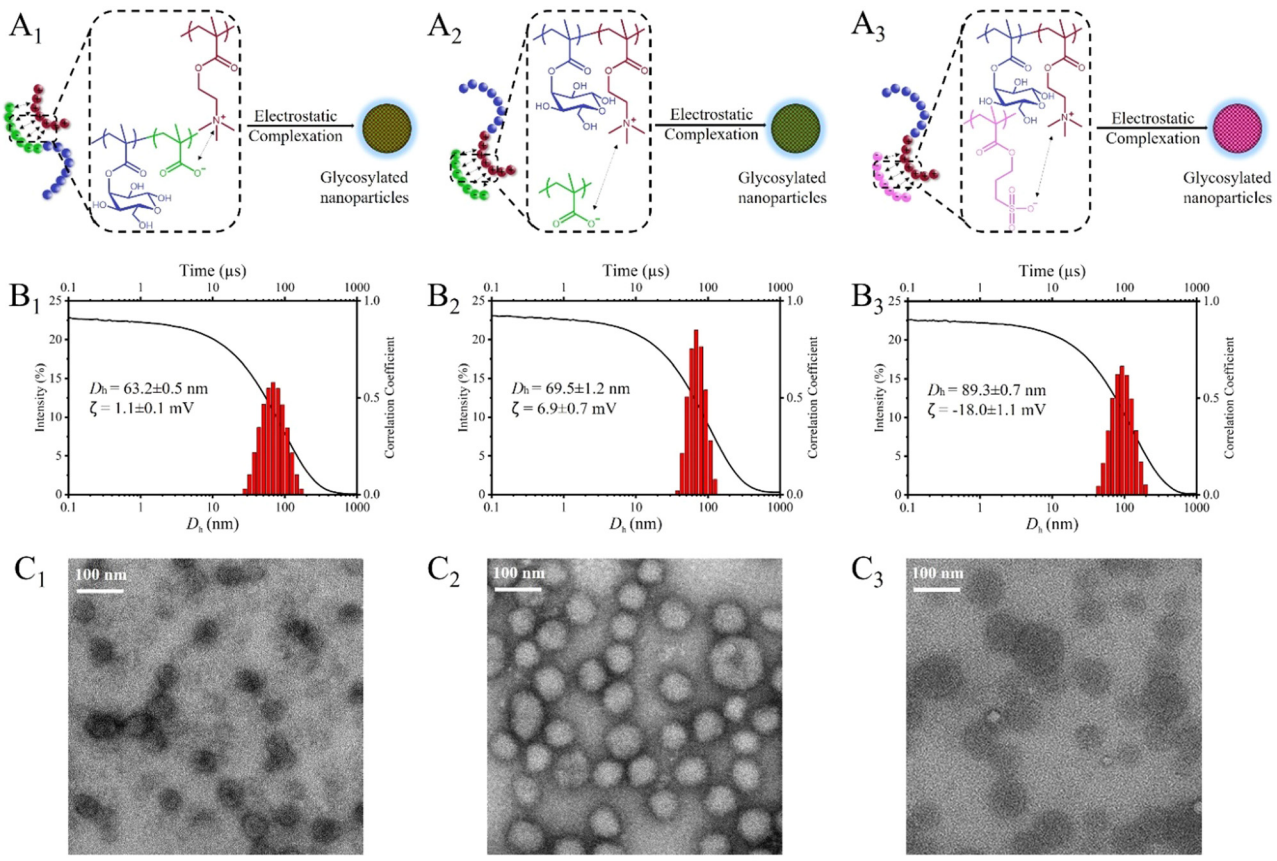

Fig. 3 Formation of glycosylated polyplex micelles using one charged glycosylated block copolymer and one oppositely charged homopolymer. Depiction of the electrostatic interaction between (A$_1$) $PGlcMA_{72}$-*b*-$PMAA_{85}$ and $PMETAI_{41}$ (GMP_2), (A$_2$) $PGlcMA_{72}$-*b*-$PMETAI_{71}$ and $PMAA_{74}$ (GMP_3) or (A$_3$) $PGlcMA_{72}$-*b*-$PMETAI_{71}$ and $PSPMA\text{-}Na_{114}$ (GMP_4) yielding glycosylated nanoparticles. (B$_1$)–(B$_3$) Corresponding DLS (173°) intensity plots (bars), correlation coefficient (lines) and zeta potential values. (C$_1$)–(C$_3$) Corresponding TEM images of uranyl acetate-stained glycosylated nanoparticles.

involves fusion-fission or expulsion-insertion events, ultimately yielding spherical polyplex micelles.

We prepared another spherical core-corona polyplex micelle by mixing $PMAA_{74}$ with $PGlcMA_{72}$-*b*-$PMETAI_{71}$ (GPM_3, Fig. $3A_2$). Like GPM_2, GPM_3 comprises a core consisting of complexed PMETAI and PMAA encapsulated by a PGlcMA corona. The DLS results (Fig. $3B_2$ and Fig. S7-3, ESI†) and TEM images (Fig. $3C_2$) confirmed the near charge neutrality (ζ_{GPM3} = 6.9 mV, Table 1) and spherical morphology of GPM_3, with a mean core diameter of $Ø_{GPM3}$ = 70.9 nm (Fig. S8-2, ESI†). Notably, the hydrodynamic radius of GPM_3 ($D_{h\,GPM3}$ = 69.5 nm, Table 1) is larger than that of GPM_2 primarily because of the increased length of the core-forming block.[62,63] The glycosylated polyplex micelles formed by the complexation of PSPMA-Na_{114}/$PGlcMA_{72}$-*b*-$PMETAI_{71}$ (GPM_4, Fig. $3A_3$) exhibited a relative large hydrodynamic radius ($D_{h\,GPM4}$ = 89.3 nm, Table 1), as confirmed by the DLS results (Fig. $3B_3$ and Fig. S7-4, ESI†). The increase in size is attributed to the larger volume and higher molar mass of PSPMA-Na than of the PMAA segment. Despite a 1 : 1 stoichiometric ratio, the ζ-potential (ζ_{GPM4} = −18.0 mV, Table 1) of GPM_4 remained negative, indicating incomplete charge compensation of PSPMA-Na units. This could be due to the larger hydrodynamic volume and stiffer nature of the PSPMA-Na chains than those of PMAA, as well as the broad dispersity of the block copolymer contributes to increased heterogeneity during micelle formation, leading to a wider size distribution an uneven ζ-potential among the nanoparticles. Although the PGlcMA corona provides stabilization, the negatively charged GPM_4 remains susceptible to aggregation, as confirmed by the TEM images (Fig. $3C_3$ and Fig. S8-3, ESI†). To achieve complete charge compensation of the PSPMA-Na units, ζ-potential titration across various charge ratios was performed (Fig. S9, ESI†). Therefore, we used a ratio of 0.5 : 1 between PSPMA-Na_{114} and $PGlcMA_{72}$-*b*-$PMETAI_{71}$ (GPM_5), and the ζ-potential (ζ_{GPM5} = −5.0 mV, Table 1) of GPM_5 confirmed the formation of a nearly charge-neutral complex core. TEM images (Fig. 4B) revealed the spherical morphology of GPM_5, with variable dimensions of the particles but less aggregation. Both the hydrodynamic radius ($D_{h\,GPM5}$ = 114.0 nm, Table 1) and mean core diameter ($Ø_{GPM5}$ = 96.2 nm) increased compared with those of GPM_4, likely due to the incorporation of additional $PGlcMA_{72}$-*b*-$PMETAI_{71}$ chains into the complex core to fully compensate for the charges of PSPMA-Na_{114}.[64] The larger hydrodynamic radius compared with the mean core diameter is attributed to the intensity-weighted averaging in DLS measurements, which is more sensitive to larger particles.[65]

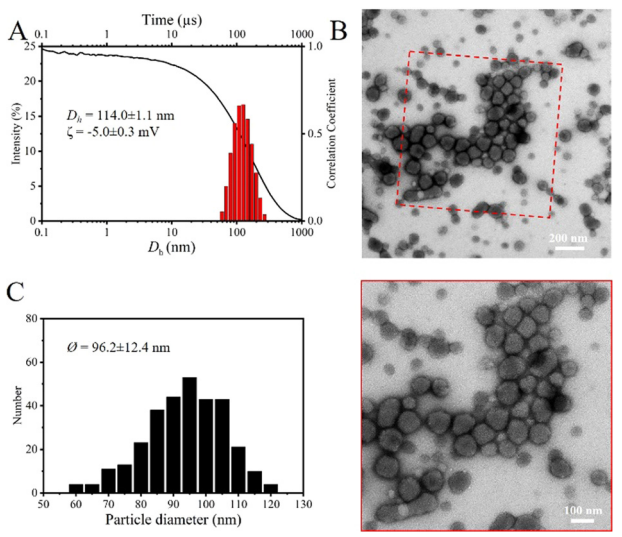

Fig. 4 Morphology analyses of GPM_5. (A) DLS (173°) intensity plots (bars), correlation coefficient (line) and zeta potential value. (B) TEM images of uranyl acetate-stained glycosylated nanoparticles. (C) Statistical analysis of glycosylated nanoparticles (data extracted from 300 particles in several images).

Conclusions

This study successfully demonstrated the potential to fabricate glycosylated polyplex micelles through electrostatic interactions. Oppositely charged block glycosylated copolymers were produced in a straightforward fashion, *via* a combination of RAFT polymerization and postpolymerization modification. Upon mixing oppositely charged block copolymers, stable nonspherical nanoparticles were formed. Their morphology was confirmed by dynamic light scattering and transmission electron microscopy, underscoring the precision of this method in the preparation of glycosylated nanoparticles. The versatility of this system was further explored by employing oppositely charged homopolymers, broadening the potential applications of glycosylated nanoparticles. This approach offers a promising pathway toward more intricate nanoparticle designs, with potential for use in responsive delivery systems and other advanced biomedical applications. The insights gained from this work pave the way for future research into the responsive characteristics of these nanoparticles, facilitating their evolution into more sophisticated carriers for therapeutic cargo.

Author contributions

The manuscript was written through the contributions of all authors. All the authors approved the final version of the manuscript. Conceptualization, M. C., T. P., J. B., V. S. D. V., R. F. and K. L.; methodology, M. C., T. P. and J. B.; writing – reviewing & editing, M. C., T. P., J. B., V. S. D. V., R. F. and K. L.; funding acquisition, V. S. D. V., R. F. and K. L.; resources, V. S. D. V., R. F. and K. L.

Data availability

The data supporting this article have been included as part of the ESI.†

Conflicts of interest

The authors declare that they have no competing financial interests.

Acknowledgements

The authors warmly thank Jur van Dijken, Dr Marc C. A. Stuart, Renze Sneep, Albert Woortman and Eleni Thomou for their technical assistance with thermogravimetric analyses, electron microscopy, HRMS and GPC, respectively. M. C. thanks Kai Lu for his assistance in analysing the morphologies of the glycosylated polyplex micelles. This research received funding from the Dutch Research Council (NWO) in the framework of the ENW PPP Fund for the top sectors and from the Ministry of Economic Affairs in the framework of the 'PPS-Toeslagregeling'. M. C. thanks financial support from a Chinese Scholarship Council grant (no. 202006240066) and University of Groningen scholarship top-up.

References

1 R. C. Saxena, D. K. Adhikari and H. B. Goyal, *Renewable Sustainable Energy Rev.*, 2009, **13**, 167–178.
2 D. J. Cosgrove, *Curr. Opin. Plant Biol.*, 2018, **46**, 77–86.
3 A. Domard, *Carbohydr. Polym.*, 2011, **84**, 696–703.
4 M. D. Shoulders and R. T. Raines, *Annu. Rev. Biochem.*, 2009, **78**, 929–958.
5 J. J. Lundquist and E. J. Toone, *Chem. Rev.*, 2002, **102**, 555–578.
6 C. S. Mahon, G. C. Wildsmith, D. Haksar, E. de Poel, J. M. Beekman, R. J. Pieters, M. E. Webb and W. B. Turnbull, *Faraday Discuss.*, 2019, **219**, 112–127.
7 W. Stuart-Walker and C. S. Mahon, *Adv. Drug Delivery Rev.*, 2021, **171**, 77–93.
8 J. Ciric and K. Loos, *Carbohydr. Polym.*, 2013, **93**, 31–37.
9 L. Boetje, X. Lan, F. Silvianti, J. van Dijken, M. Polhuis and K. Loos, *Carbohydr. Polym.*, 2022, **292**, 119649.
10 X. Lan, W. Li, C. Ye, L. Boetje, T. Pelras, F. Silvianti, Q. Chen, Y. Pei and K. Loos, *ACS Appl. Mater. Interfaces*, 2023, **15**, 4398–4407.
11 K. Loos, G. Jonas and R. Stadler, *Macromol. Chem. Phys.*, 2001, **202**, 3210–3218.
12 T. Pelras and K. Loos, *Prog. Polym. Sci.*, 2021, **117**, 101393.
13 A. Adharis, T. Ketelaar, A. G. Komarudin and K. Loos, *Biomacromolecules*, 2019, **20**, 1325–1333.
14 A. Adharis, D. Vesper, N. Koning and K. Loos, *Green Chem.*, 2018, **20**, 476–484.
15 A. Adharis and K. Loos, *Macromol. Chem. Phys.*, 2019, **220**, 1900219.
16 W. M. J. Kloosterman, D. Jovanovic, S. G. M. Brouwer and K. Loos, *Green Chem.*, 2014, **16**, 203–210.
17 C. Cao, J. Zhao, M. Lu, C. J. Garvey and M. H. Stenzel, *Biomacromolecules*, 2019, **20**, 1545–1554.
18 E. Prochazkova, C. Cao, A. Rawal, M. Dracinsky, S. Bhattacharyya, I. Cisarova, J. M. Hook and M. H. Stenzel, *ACS Appl. Mater. Interfaces*, 2019, **11**, 28278–28288.
19 C. Cao, J. Zhao, F. Chen, M. Lu, Y. Y. Khine, A. Macmillan, C. J. Garvey and M. H. Stenzel, *Chem. Mater.*, 2018, **30**, 5227–5236.
20 S. Ganda, Y. Jiang, D. S. Thomas, J. Eliezar and M. H. Stenzel, *Macromolecules*, 2016, **49**, 4136–4146.
21 H. Schlaad, L. You, R. Sigel, B. Smarsly, M. Heydenreich, A. Mantion and A. Masic, *Chem. Commun.*, 2009, 1478–1480.
22 Z. Hordyjewcz-Baran, L. You, B. Smarsly, R. Sigel and H. Schlaad, *Macromolecules*, 2007, **40**, 3901–3903.
23 L. You and H. Schlaad, *J. Am. Chem. Soc.*, 2006, **128**, 13336–13337.
24 V. Ladmiral, M. Semsarilar, I. Canton and S. P. Armes, *J. Am. Chem. Soc.*, 2013, **135**, 13574–13581.
25 L. Qiu, H. Zhang, T. Bick, J. Martin, P. Wendler, A. Boker, U. Glebe and C. Xing, *Angew. Chem., Int. Ed.*, 2021, **60**, 11098–11103.
26 W. Qi, Y. Zhang, J. Wang, G. Tao, L. Wu, Z. Kochovski, H. Gao, G. Chen and M. Jiang, *J. Am. Chem. Soc.*, 2018, **140**, 8851–8857.
27 X. Wu, L. Su, G. Chen and M. Jiang, *Macromolecules*, 2015, **48**, 3705–3712.
28 L. Su, C. Wang, F. Polzer, Y. Lu, G. Chen and M. Jiang, *ACS Macro Lett.*, 2014, **3**, 534–539.
29 L. Su, Y. Zhao, G. Chen and M. Jiang, *Polym. Chem.*, 2012, **3**, 1560–1566.
30 G. Pasparakis and C. Alexander, *Angew. Chem., Int. Ed.*, 2008, **120**, 4925–4928.
31 D. V. Pergushov, E. V. Remizova, J. Feldthusen, A. B. Zezin, A. H. E. Müller and V. A. Kabanov, *J. Phys. Chem. B*, 2003, **107**, 8093–8096.
32 Y. Li, T. K. Bronich, P. S. Chelushkin and A. V. Kabanov, *Macromolecules*, 2008, **41**, 5863–5868.
33 J. Sun and Z. Li, *Macromolecules*, 2020, **53**, 8737–8740.
34 M. Ibrahim, E. Ramadan, N. E. Elsadek, S. E. Emam, T. Shimizu, H. Ando, Y. Ishima, O. H. Elgarhy, H. A. Sarhan, A. K. Hussein and T. Ishida, *J. Controlled Release*, 2022, **351**, 215–230.
35 R. P. Garay, R. El-Gewely, J. K. Armstrong, G. Garratty and P. Richette, *Expert Opin. Drug. Delivery*, 2012, **9**, 1319–1323.
36 W. M. J. Kloosterman, S. Roest, S. R. Priatna, E. Stavila and K. Loos, *Green Chem.*, 2014, **16**, 1837–1846.
37 E. F. Fiandra, L. Shaw, M. Starck, C. J. McGurk and C. S. Mahon, *Chem. Soc. Rev.*, 2023, **52**, 8085–8105.
38 A. Monaco, V. P. Beyer, R. Napier and C. R. Becer, *Biomacromolecules*, 2020, **21**, 3736–3744.
39 T. Tanaka, A. Matsuura, Y. Aso and H. Ohara, *Chem. Commun.*, 2020, **56**, 10321–10324.
40 E. L. Sahkulubey Kahveci, M. U. Kahveci, A. Celebi, T. Avsar and S. Derman, *Biomacromolecules*, 2022, **23**, 4896–4908.
41 J. Zhao, H. Lu, Y. Yao, S. Ganda and M. H. Stenzel, *J. Mater. Chem. B*, 2018, **6**, 4223–4231.
42 S. Ganda, M. Dulle, M. Drechsler, B. Förster, S. Förster and M. H. Stenzel, *Macromolecules*, 2017, **50**, 8544–8553.
43 M. Lu, F. Chen, C. Cao, C. J. Garvey, N. L. Fletcher, Z. H. Houston, H. Lu, M. S. Lord, K. J. Thurecht and M. H. Stenzel, *Macromolecules*, 2019, **52**, 477–486.
44 A. H. Hofman, R. Fokkink and M. Kamperman, *Polym. Chem.*, 2019, **10**, 6109–6115.

45 A. D. Filippov, I. A. van Hees, R. Fokkink, I. K. Voets and M. Kamperman, *Macromolecules*, 2018, **51**, 8316–8323.
46 A. Dag, M. Callari, H. Lu and M. H. Stenzel, *Polym. Chem.*, 2016, **7**, 1031–1036.
47 T. Pelras, C. S. Mahon Nonappa, O. Ikkala, A. H. Groschel and M. Mullner, *J. Am. Chem. Soc.*, 2018, **140**, 12736–12740.
48 T. Pelras Nonappa, C. S. Mahon and M. Müllner, *Macromol. Rapid Commun.*, 2020, **42**, 2000401.
49 M. Vamvakaki, G.-F. Unali, V. Bütün, S. Boucher, K. L. Robinson, N. C. Billingham and S. P. Armes, *Macromolecules*, 2001, **34**, 6839–6841.
50 J. H. Lai, *Macromolecules*, 1984, **17**, 1010–1012.
51 L. Leibler, *Macromolecules*, 1980, **13**, 1602–1617.
52 A. L. Patterson, S. P. O. Danielsen, B. Yu, E. C. Davidson, G. H. Fredrickson and R. A. Segalman, *Macromolecules*, 2019, **52**, 1277–1286.
53 T. Swift, L. Swanson, M. Geoghegan and S. Rimmer, *Soft Matter*, 2016, **12**, 2542–2549.
54 D. V. Pergushov, A. H. Müller and F. H. Schacher, *Chem. Soc. Rev.*, 2012, **41**, 6888–6901.
55 M. Sedlák, *J. Chem. Phys.*, 2002, **116**, 5256–5262.
56 C. A. Scarff, M. J. G. Fuller, R. F. Thompson and M. G. Iadanza, *J. Visualized Exp.*, 2018, **6**, 57199.
57 J. C. Eriksson and S. Ljunggren, *Langmuir*, 2000, **6**, 895–904.
58 I. K. Voets, A. de Keizer, P. de Waard, P. M. Frederik, P. H. Bomans, H. Schmalz, A. Walther, S. M. King, F. A. Leermakers and M. A. Cohen Stuart, *Angew. Chem., Int. Ed.*, 2006, **45**, 6673–6676.
59 I. K. Voets, R. Fokkink, T. Hellweg, S. M. King, P. de Waard, A. de Keizer and M. A. C. Stuar, *Soft Matter*, 2009, **5**, 999–1005.
60 M. Amann, J. S. Diget, J. Lyngsø, J. S. Pedersen, T. Narayanan and R. Lund, *Macromolecules*, 2019, **52**, 8227–8237.
61 C. C. M. Sproncken, J. R. Magana and I. K. Voets, *ACS Macro Lett.*, 2021, **10**, 167–179.
62 S. V. D. Burgh, A. D. Keizer and M. A. C. Stuart, *Langmuir*, 2004, (20), 1073–1084.
63 H. M. van der Kooij, E. Spruijt, I. K. Voets, R. Fokkink, M. A. Cohen Stuart and J. van der Gucht, *Langmuir*, 2012, **28**, 14180–14191.
64 H. E. Cingil, E. B. Boz, J. Wang, M. A. C. Stuart and J. Sprakel, *Adv. Funct. Mater.*, 2016, **26**, 1420–1427.
65 S. Bhattacharjee, *J. Controlled Release*, 2016, **235**, 337–351.